Supporting Information

Exsolution of SrO during the topochemical conversion of $LaSr_3CoRuO_8$ to the oxyhydride $LaSr_3CoRuO_4H_4$

Lun Jin[†], Maria Batuk[‡], Franziska K. K. Kirschner[⊗], Franz Lang[⊗], Stephen J. Blundell[⊗], Joke Hadermann[‡] and Michael A. Hayward[†]*

Table of Contents

1. Strucutral characterization of $LaSr_3CoRuO_8$

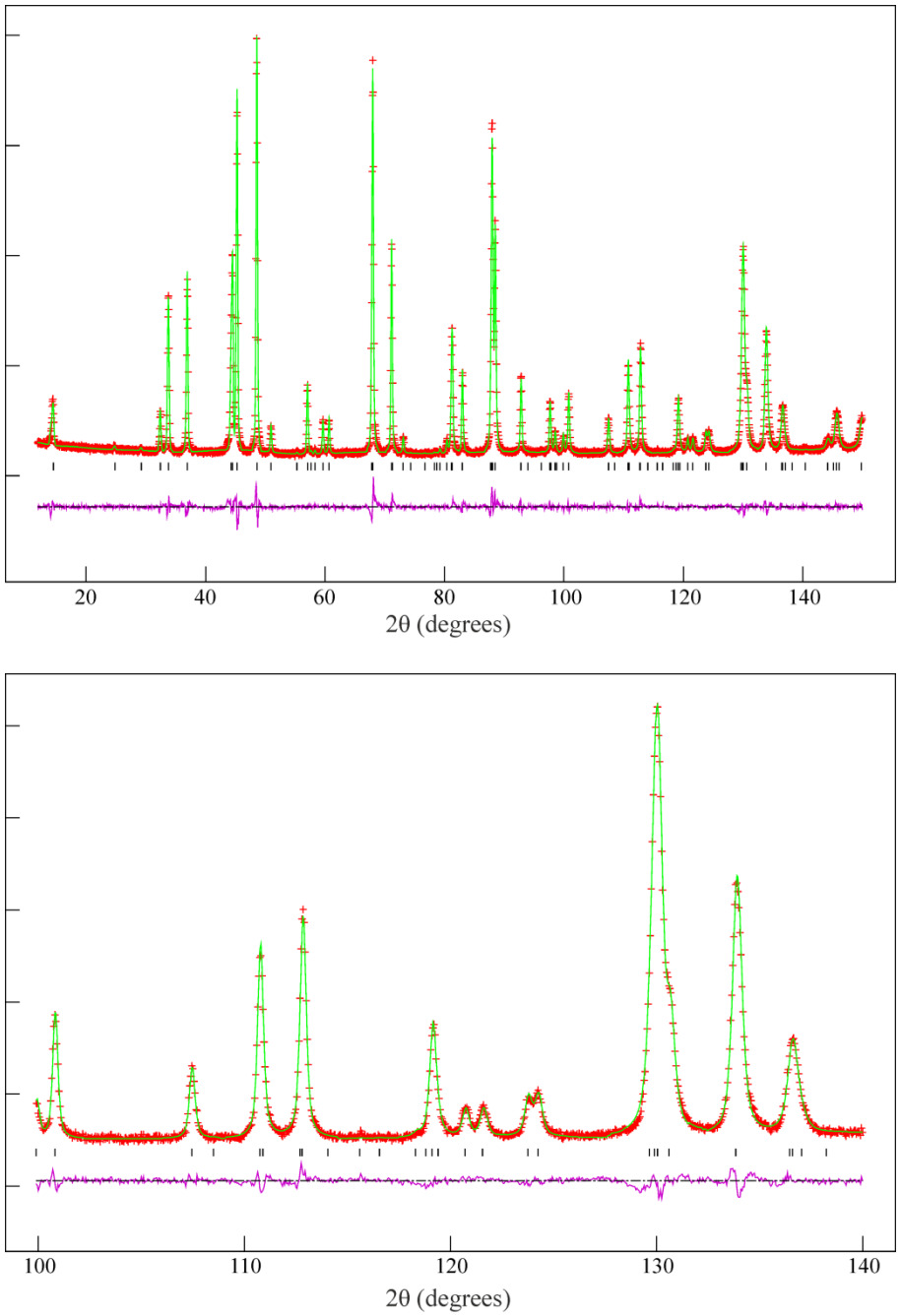

Figure S1. Observed calculated and difference plots from the structural refinement of $LaSr_3CoRuO_8$ against neutron powder diffraction data. Lower panel shows expanded region $100 < 2\theta < 140$ to emphasize there is no indication of any intergrowths in this material.

Atom	Site	*x*	*y*	*z*	Fraction	U_{iso} equiv. (Å^2)
La/Sr(1)	4*e*	0	0	0.3561(1)	0.25/0.75	0.0049
Co/Ru(1)	2*a*	0	0	0	0.5/0.5	0.0021
O(1)	4*e*	0	0	0.1636(1)	1	0.0124
O(2)	4*c*	0.5	0	0	1	0.0058
$LaSr_3CoRuO_8$ space group *I*4/*mmm* (#139) Formula weight : 689.76 g mol^{-1}, Z = 2 *a* = 3.87488(4) Å, *c* = 12.6258(1) Å, Volume = 189.574(7) Å^3						
Radiation source: Neutron Powder Diffraction, λ = 1.5943(2) Temperature: 298 K χ^2 = 4.132; *wRp* = 4.90%; *Rp* = 3.73%.						

Table S1. Parameters from the strucutral refinement of $LaSr_3CoRuO_8$ against neutron powder diffraction data collected at 298 K.

Atom	U_{11}	U_{22}	U_{33}
La/Sr(1)	0.0065(3)	0.0065(3)	0.0014(5)
Co/Ru(1)	0.0018(4)	0.0018(4)	0.0024(2)
O(1)	0.0131(4)	0.0131(4)	0.0107(1)
O(2)	0.0040(6)	0.0054(7)	0.0079(7)

Table S2. Anisotropic displacement parameters from the strucutral refinement of $LaSr_3CoRuO_8$ against neutron powder diffraction data collected at 298 K.

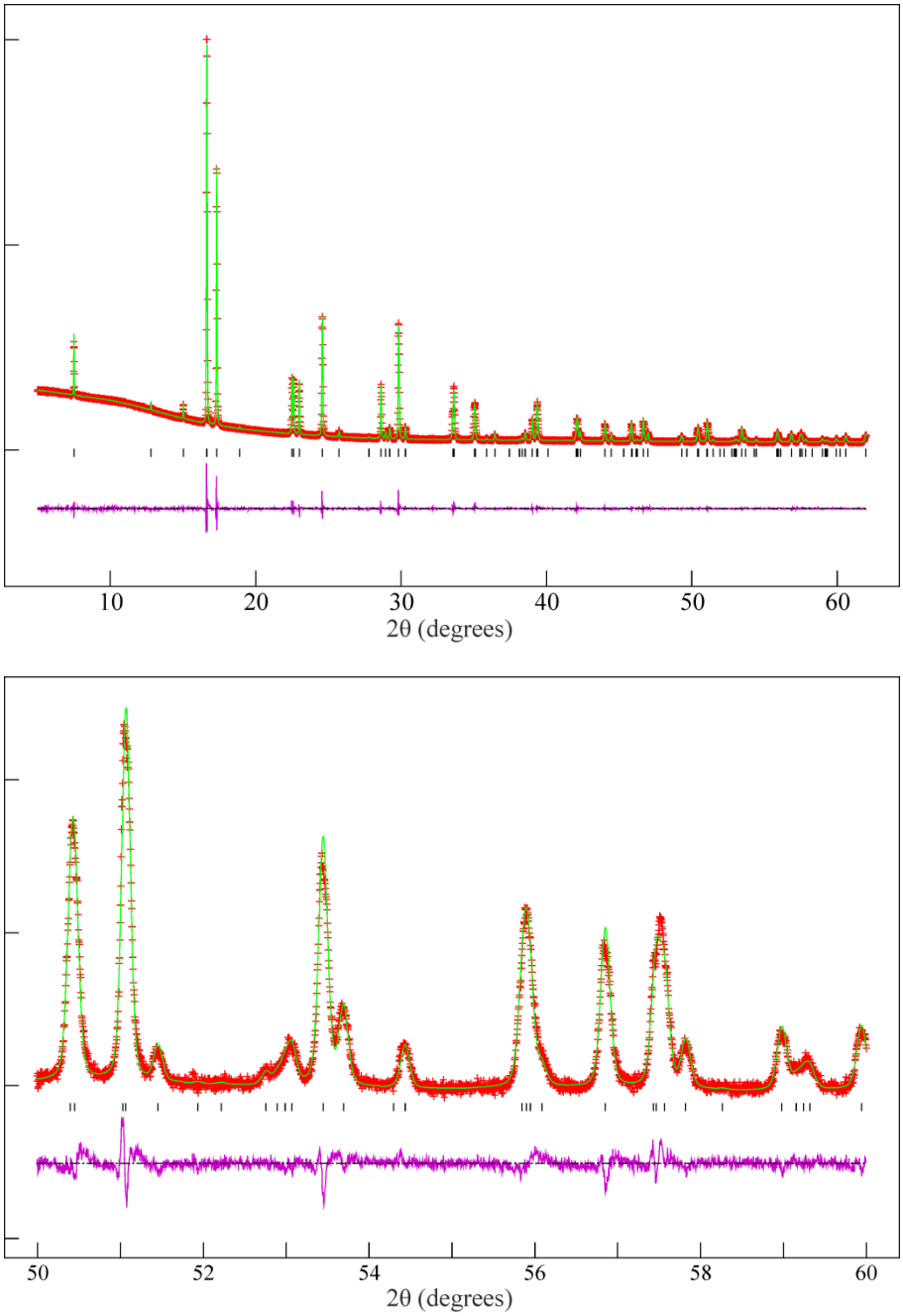

Figure S2. Observed calculated and difference plots from the structural refinement of $LaSr_3CoRuO_8$ against synchrotron X-ray powder diffraction data. Lower panel shows expanded region $50 < 2\theta < 60$ to emphasize there is no indication of any intergrowths in this material.

2. Strucutral Characterization of '$LaSr_3CoRuO_4H_4$'

Atom	Site	*x*	*y*	*z*	Fraction	U_{iso} equiv.(Å^2)
La/Sr(1)	4*e*	0	0	0.3513(1)	0.25/0.75	0.0174
Co/Ru(1)	2*a*	0	0	0	0.5/0.5	0.0250
O(1)	4*e*	0	0	0.1655(2)	1	0.0198
H(1)	4*c*	0.5	0	0	1	0.1379
$LaSr_3CoRuO_4H_4$ space group *I*4/*mmm* (#139) Formula weight : 629.80 g mol^{-1}, Z = 2 Mass fraction: 88.9(2)% *a* = 3.6484(3) Å, *c* = 13.353(1) Å, Volume = 177.75(4) Å^3						
$LaSr_3CoRuO_{6\pm x}$ space group *Immm* (#71) Formula weight : 657.76 ± δ g mol^{-1}, Z = 2 Mass fraction: 12.1(1)% *a* = 3.8071(6) Å, *b* = 3.6161(6) Å, *c* = 13.172(1) Å, Volume = 181.35(5) Å^3						
Radiation source: Neutron time of flight Temperature: 298 K χ^2 = 18.72; *wRp*= 2.96%; *Rp* = 1.76%.						

Table S3. Structural parameters from the refinement of neutron powder diffraction data collected from $LaSr_3CoRuO_4H_4$ at 298 K.

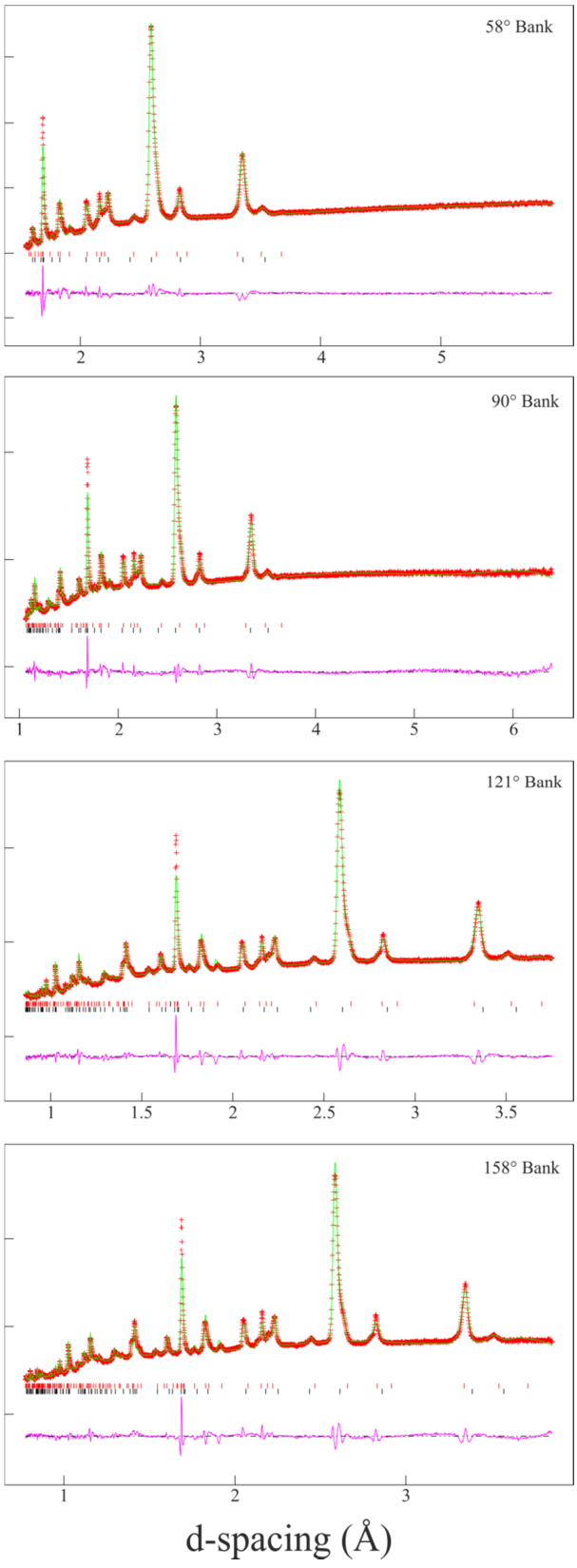

Figure S3. Observed, calculated and difference plots from the strucutral refinement of $LaSr_3CoRuO_4H_4$ (space group *I*4/*mmm*) against neutron powder diffraction data collected at 298 K. Tick marks indicate peak positions of the majority phase (black) and the minority phase $LaSr_3CoRuO_{6\pm x}$ (red).

3. Microstrucutral characterization of '$LaSr_3CoRuO_4H_4$'

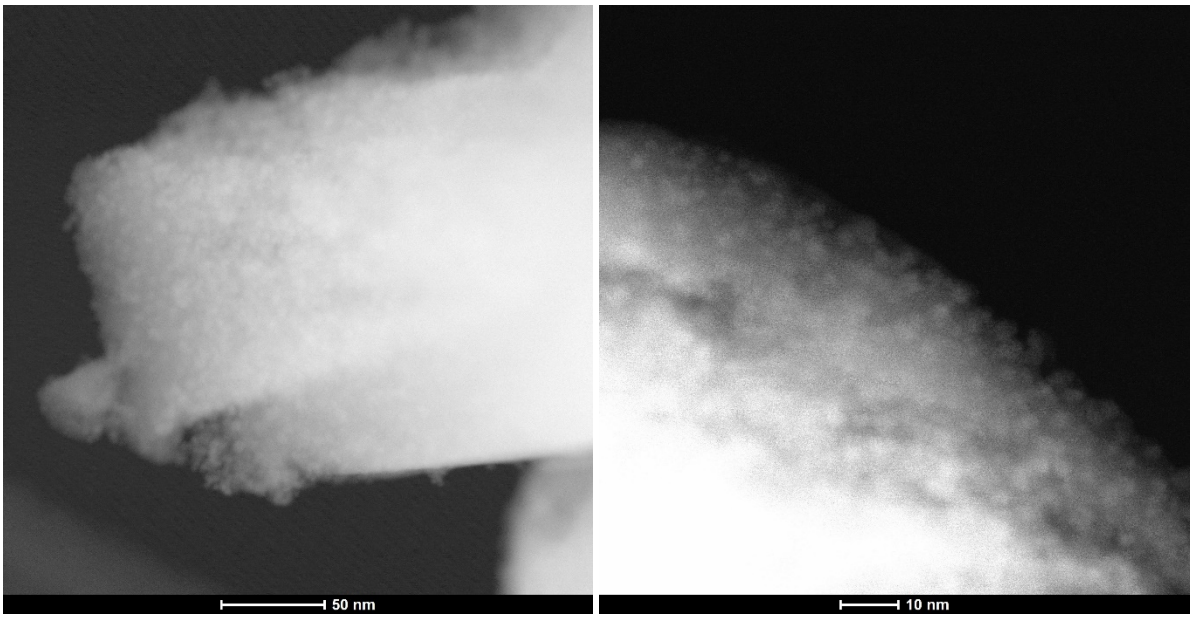

Figure S4. HAADF-STEM images of the crystallites of Sample C covered with nanoparticles.

4. Faults simulation model.

The layers that make up the FAULTS model are defined relative to a set of common lattice parameters.

Average cell: a = 3.63 Å, b = 3.63Å, c = 3.98 Å

Layer 1, n =1 $LaSr_3CoRuO_4H_4$ layer

Atom	*x*	*y*	*z*	Fraction
La/Sr	0	0	0	0.25/0.75
Co/Ru	½	½	½	0.5/0.5
O	½	½	-0.067	1
H	½	0	0.5	1
H	0	½	0.5	1
La/Sr	0	0	1	0.25/0.75
O	½	½	1.067	1

Layer 2, n = 2 $LaSr_2CoRuO_3H_4$ layer

Atom	*x*	*y*	*z*	Fraction
La/Sr	0	0	0	0.25/0.75
O	½	½	0	1
Co/Ru	½	½	0.485	0.5/0.5
H	½	0	0.485	1
H	0	½	0.485	1
La/Sr	0	0	0.970	0.5/0.5
O	½	½	0.970	1
Co/Ru	½	½	1.45	0.5/0.5
H	½	0	1.45	1
H	0	½	1.45	1
La/Sr	0	0	1.94	0.25/0.75
O	½	½	1.94	1

Arrays for stacked layers are created by stacking layer 1 and layer 2 depending on the transition probability (1 → 1, 1→ 2, 2 → 1 and 2 → 2) and a stacking vector, expressed as a fraction of the average unit cell, which defines the relative positions of the origins of adjacent layers.

The ‘isolated defect’ and ‘aggregated defect’ simulations used the same constituent layers, but different stacking probabilities, as shown below.

Isolated defect stacking model

Layer A	Layer B	Probability (%)	stacking vector		
			x	*y*	*z*
1	1	100	0.5	0.5	1.67
1	2	0	0.5	0.5	1.67
2	1	100	0.5	0.5	2.67
2	2	0	0.5	0.5	2.67

100% Layer 1, 0% Layer 2

Layer A	Layer B	Probability (%)	stacking vector		
			x	*y*	*z*
1	1	98	0.5	0.5	1.67
1	2	2	0.5	0.5	1.67
2	1	100	0.5	0.5	2.67
2	2	0	0.5	0.5	2.67

98% Layer 1, 2% Layer 2

Layer A	Layer B	Probability (%)	stacking vector		
			x	*y*	*z*
1	1	95	0.5	0.5	1.67
1	2	5	0.5	0.5	1.67
2	1	100	0.5	0.5	2.67
2	2	0	0.5	0.5	2.67

95% Layer 1, 5% Layer 2

Layer A	Layer B	Probability (%)	stacking vector		
			x	*y*	*z*
1	1	91	0.5	0.5	1.67
1	2	9	0.5	0.5	1.67
2	1	100	0.5	0.5	2.67
2	2	0	0.5	0.5	2.67

91% Layer 1, 9% Layer 2

Aggregated defect stacking model

Layer A	Layer B	Probability (%)	stacking vector		
			x	*y*	*z*
1	1	85	0.5	0.5	1.67
1	2	15	0.5	0.5	1.67
2	1	100	0.5	0.5	2.67
2	2	0	0.5	0.5	2.67

85% Layer 1, 14% Layer 2

Layer A	Layer B	Probability (%)	stacking vector		
			x	*y*	*z*
1	1	87.2	0.5	0.5	1.67
1	2	12.8	0.5	0.5	1.67
2	1	75	0.5	0.5	2.67
2	2	25	0.5	0.5	2.67

25% aggregation, 85% Layer 1, 14% Layer 2

Layer A	Layer B	Probability (%)	stacking vector		
			x	*y*	*z*
1	1	91.5	0.5	0.5	1.67
1	2	8.5	0.5	0.5	1.67
2	1	50	0.5	0.5	2.67
2	2	50	0.5	0.5	2.67

50% aggregation, 85% Layer 1, 14% Layer 2

Layer A	Layer B	Probability (%)	stacking vector		
			x	*y*	*z*
1	1	95	0.5	0.5	1.67
1	2	5	0.5	0.5	1.67
2	1	30	0.5	0.5	2.67
2	2	70	0.5	0.5	2.67

70% aggregation, 85% Layer 1, 14% Layer 2

5. Magnetic Characterization of '$LaSr_3CoRuO_4H_4$'

Procedure used to measure the magnetization of samples containing elemental cobalt:
The magnetization of elemental cobalt is observed to saturate in applied magnetic fields of more than 3 T. Thus the paramagnetic susceptibility of a bulk sample can be measured in the presence of elemental cobalt impurities by measuring the gradient of magnetization-field isotherms in applied fields larger than 3 T. As shown in Figure S5.

To this end the magnetization of samples was measured in a series of 5 fields between 3 T and 5 T. The magnetization vs. field data were fitted to a linear function, the gradient of which is the paramagnetic susceptibility of the bulk sample and the intercept is the saturated ferromagnetic moment of the sample. Data points with large errors were excluded from fits. All fits had at least 5 data points. This procedure was repeated at 5 K intervals between 5 K and 300 K to measure the temperature dependent susceptibility of samples.

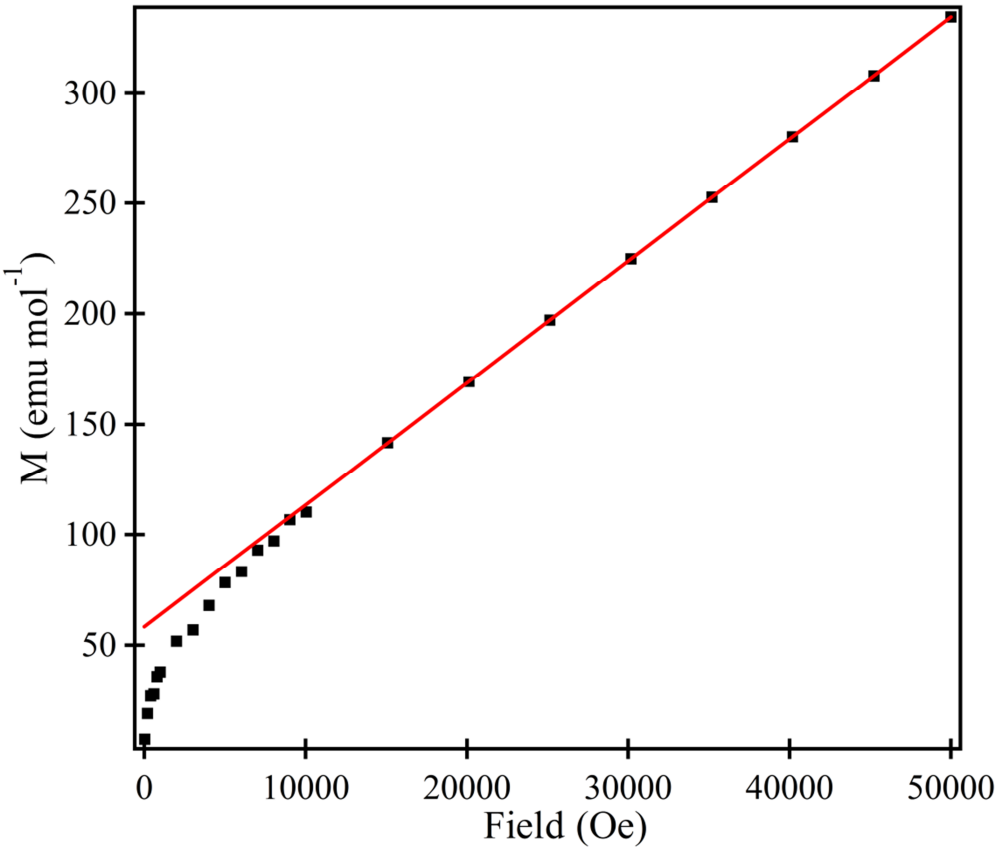

Figure S5. Magnetisation of a $LaSr_3CoRuO_4H_4$ sample measured as a function of applied field at 300 K. A linear fit to high-field region (H > 30000 Oe) yields a gradient which is the paramagnetic susceptibility of the sample, and an intercept which is the saturated ferromagnetic moment of the sample.

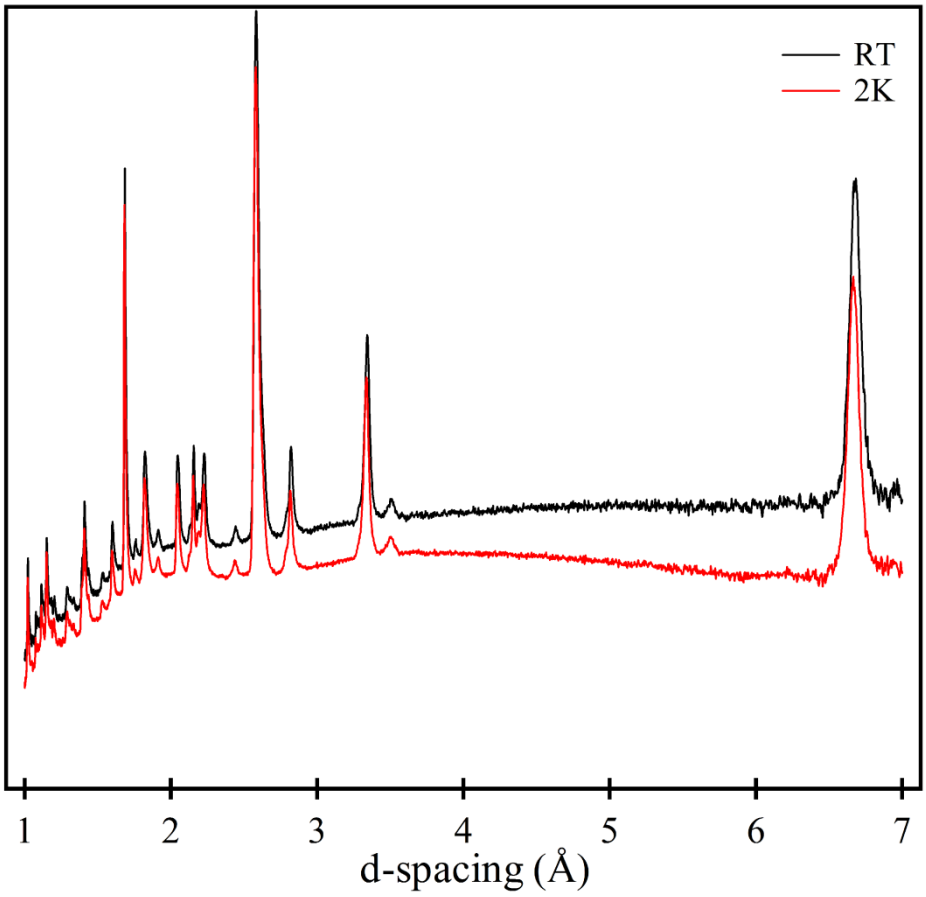

Figure S6. Plots of neutron powder diffraction data collected from sample B of '$LaSr_3CoRuO_4H_4$' at ambient temperture and 2 K using the 90º detector bank of the WISH diffractometer.